NanoSIMS imaging reveals metabolic stratification within current-producing biofilms

Grayson L. Chadwick[a,1], Fernanda Jiménez Otero[b,1], Jeffrey A. Gralnick[b,c], Daniel R. Bond[b,c,2], and Victoria J. Orphan[a,2]

[a]Division of Geological and Planetary Sciences, California Institute of Technology, Pasadena, CA 91125; [b]BioTechnology Institute, University of Minnesota, Saint Paul, MN 55108; and [c]Department of Plant and Microbial Biology, University of Minnesota, Saint Paul, MN 55108

Edited by Susan L. Brantley, Pennsylvania State University, University Park, PA, and approved August 29, 2019 (received for review July 24, 2019)

Metal-reducing bacteria direct electrons to their outer surfaces, where insoluble metal oxides or electrodes act as terminal electron acceptors, generating electrical current from anaerobic respiration. *Geobacter sulfurreducens* is a commonly enriched electricity-producing organism, forming thick conductive biofilms that magnify total activity by supporting respiration of cells not in direct contact with electrodes. Hypotheses explaining why these biofilms fail to produce higher current densities suggest inhibition by formation of pH, nutrient, or redox potential gradients; but these explanations are often contradictory, and a lack of direct measurements of cellular growth within biofilms prevents discrimination between these models. To address this fundamental question, we measured the anabolic activity of *G. sulfurreducens* biofilms using stable isotope probing coupled to nanoscale secondary ion mass spectrometry (nanoSIMS). Our results demonstrate that the most active cells are at the anode surface, and that this activity decreases with distance, reaching a minimum 10 μm from the electrode. Cells nearest the electrode continue to grow at their maximum rate in weeks-old biofilms 80-μm-thick, indicating nutrient or buffer diffusion into the biofilm is not rate-limiting. This pattern, where highest activity occurs at the electrode and declines with each cell layer, is present in thin biofilms (<5 μm) and fully grown biofilms (>20 μm), and at different anode redox potentials. These results suggest a growth penalty is associated with respiring insoluble electron acceptors at micron distances, which has important implications for improving microbial electrochemical devices as well as our understanding of syntrophic associations harnessing the phenomenon of microbial conductivity.

Geobacter sulfurreducens | nanoSIMS | extracellular electron transfer | electrode reduction | stable isotope tracers

Microbial communities in nature exist predominantly as biofilms (1, 2). These dense cell aggregates coat mineral surfaces and multicellular organisms in aquatic environments, sediments, soils, and the subsurface, controlling the majority of metal, sulfur, nitrogen, and carbon cycling (3–6). Due to their high cell densities, diffusion of buffering agents and respiratory substrates to inner layers is limited (1, 7–11). Stratification of biofilms into phenotypically (12) and metabolically (13) separate regions is well-documented, creating structured microhabitats that alter respiration of organic matter (5), biodegradation of substrates (14), and inhibition by antibiotics (2).

Biofilms composed of metal-reducing bacteria represent a special case, as a subset of these organisms create between-cell conductive pathways directing electrons to acceptors many microns away. Electrodes colonized by such bacteria can oxidize organic wastes or power remote devices in a host of new electrochemical technologies, but the fundamental limits to conductive electrode biofilm metabolic activity are not understood (15). Unlike biofilms growing on a surface, where cells near the medium interface have optimal access to nutrients, a conductive community faces a paradox; cell layers close to an electrode have best access to the electron acceptor, but those farther from the electrode have best access to soluble electron donors and buffering agents diffusing in from the medium (16). If conductivity is rate-limiting, cell metabolism should be most rapid near the electrode. If diffusion is limiting, most cell activity is hypothesized to occur near the top.

Geobacter sulfurreducens is a model organism used to study extracellular electron transfer and biofilm conductivity (16–21), as it can be grown using solid anodes or insoluble metal oxides, or in syntrophic granules with other bacteria as terminal electron acceptors (22). Under optimal conditions with a suitably poised electrode, *G. sulfurreducens* will form conductive biofilms over 20 cell layers thick within 3 d and produce current densities on the order of 1 $mA{\cdot}cm^{-2}$ (23–26). A universal observation during *G. sulfurreducens* electrode experiments is that in the early stages of colonization, each new layer of cells results in a nearly proportional increase in total electrical current, suggesting that the first few layers have sufficient access to both medium nutrients and electron disposal pathways. As biofilm thickness exceeds about 10 μm, however, the addition of new biomass fails to proportionally increase total current (27, 28). Despite its importance in engineering better water treatment technologies and improving anaerobic digestion, the location of the active cell population, and the fundamental limitation controlling electrical current production in these communities, remains unknown.

The most common method used to detect stratification within electrode biofilms is cell viability staining in conjunction with

Significance

Electricity-producing bacteria are potential power sources, fermentation platforms, and desalination systems, if current densities could be increased. These organisms form conductive biofilms on electrodes, allowing new cell layers to contribute to current production until a limit is reached, but the biological underpinning of this limit is not well-understood. We investigated the limitation behind this phenomenon using stable isotope probing and nanoscale secondary ion mass spectrometry, showing active cells are restricted to layers closest to the electrode. This metabolic observation fundamentally changes our understanding of electron flow and cell growth within current-producing biofilms and provides constraints on the physical structure of natural communities reliant on this process for growth. We predict improvements in biofilm conductivity will yield higher current-producing systems.

Author contributions: G.L.C., F.J.O., J.A.G., D.R.B., and V.J.O. designed research; G.L.C. and F.J.O. performed research; G.L.C. and F.J.O. analyzed data; and G.L.C., F.J.O., J.A.G., D.R.B., and V.J.O. wrote the paper.

The authors declare no conflict of interest.

This article is a PNAS Direct Submission.

This open access article is distributed under Creative Commons Attribution-NonCommercial-NoDerivatives License 4.0 (CC BY-NC-ND).

[1]G.L.C. and F.J.O. contributed equally to this work.

[2]To whom correspondence may be addressed. Email: dbond@umn.edu or vorphan@gps.caltech.edu.

This article contains supporting information online at www.pnas.org/lookup/suppl/doi:10.1073/pnas.1912498116/-/DCSupplemental.

First Published September 23, 2019.

confocal microscopy. These methods, based on dyes that bind DNA in cells with intact or compromised membranes, yield conflicting results. Many studies report dead-staining cells near the anode surface, and live-staining cells at the interface with growth medium (23, 28, 29). However, others find the opposite, with live-staining cells at the anode and dead-staining cells distant from the electrode (30, 31), or observe live-staining cells throughout (32–34). A limitation of the stain-based approach is that positively charged propidium meant to indicate "dead" cells will accumulate inside live respiring cells in response to high membrane potential (35) and DNA-based dyes bind to extracellular nucleic acids often present in biofilms, confounding attempts to resolve the central question of where metabolic activity is occurring.

Long-range electron transfer from cells to electrodes requires active metabolism coupled to a complex conductive matrix composed of pili (32), multiheme *c*-type cytochromes (24, 26, 36), and polysaccharides (37), and studies have attempted to detect metabolic stratification by measuring expression of key genes within biofilms. Through physical separation of inner (0 to 20 μm) from outer (20 to 40 μm) biofilm layers followed by microarray analysis (38), a modest down-regulation in genes associated with metabolic activity was detected in outer biofilm layers. In contrast, fluorescent proteins driven by promoters for cytochromes, pili, or TCA cycle genes did not reveal significant differentiation between inner and outer layers in *G. sulfurreducens* electrode biofilms imaged by confocal microscopy (34).

While imaging and transcriptional methods have produced conflicting results, approaches focused on *c*-type cytochrome oxidation state or redox potential within *G. sulfurreducens* biofilms consistently reveal gradients that suggest increased activity near the electrode. Multiheme *c*-type cytochromes have characteristic UV/vis and Raman spectroscopic signatures when in oxidized vs. reduced states, enabling measurement of cytochrome oxidation state using either visual light (39, 40) or confocal Raman microscopy (41–43). These spectral studies demonstrate that *G. sulfurreducens* catabolic activity results in reduction of cytochromes, and reveal a higher ratio of reduced cytochromes in layers farther from the anode surface. Measurements using microelectrodes mirror Raman-based cytochrome profiles, showing that redox potential also becomes lower with distance from the anode surface (44). While not direct assessments of cellular activity per se, reduced cytochromes and lower redox potential should limit metabolic activity of cells farther from the electrode.

The opposite conclusion is proposed based on modeling of pH gradients within current-producing biofilms. Substrate oxidation coupled to electron removal at the electrode produces protons that must diffuse out of the biofilm, and many models predict pH levels should become inhibitory close to the electrode surface. Measurements with pH-sensitive dyes (45) or microelectrodes (44) have confirmed pH can decrease slightly from the outer surface of a thick (>50-μm) biofilm to an anode surface, where it could become inhibitory. While most models suggest diffusion of electron donors should be adequate in all regions of the biofilm (46), measurements of acetate concentrations within a very thick (>100-μm) *G. sulfurreducens* biofilm using NMR (47) detected a gradual decrease in acetate concentration from the bulk solution to the base of the biofilm, further indicating a diffusional limitation could occur near the electrode.

Sophisticated biofilm models and indirect measurements continue to predict these contradictory hypotheses, ranging from the idea of active biomass near the anode surface becoming limited by conductivity as cells grow farther out (48), vs. a nearly opposite configuration where pH- or nutrient-dependent effects limit growth near the anode (46). The recent discovery of multiple redox potential-specific electron transfer pathways in *G. sulfurreducens* (49–51) raises a third possibility, that microhabitats within the biofilm support different populations of cells utilizing different metabolic machinery, allowing uniform growth throughout analogous to metabolic differentiation reported in *Shewanella* biofilms (52). This leaves open the fundamental mystery of what restricts cell growth in conductive microbial communities that depend on extracellular electron transfer.

To conclusively identify regions of growth within electrode-reducing biofilms and test the hypothesis that metabolic stratification occurs, we directly imaged *G. sulfurreducens* anabolic activity in biofilms at subcellular resolution by coupling stable isotope probing with nanoscale secondary ion mass spectrometry (nanoSIMS). Biofilms were grown on polished graphite electrodes at 2 different redox potentials under conditions optimized to reproducibly capture cells during exponential current increase at a very early stage (~5-μm thickness), after the onset of current plateau (~20-μm), and after 2 wk of continuous biofilm accumulation (~80-μm) (25, 53). These experimental conditions are highly reproducible and have been shown to produce biofilms expressing all of the conductive components common to *G. sulfurreducens* biofilms reported in the literature (54, 55). At these various points in biofilm development, standard growth medium was substituted for stable isotope-enriched medium containing ^{15}N-enriched ammonium as the N source, ^{13}C-enriched acetate as the C source and electron donor, and ^{2}H-enriched water serving as a passive tracer of anabolism (56). ^{15}N, ^{13}C, and ^{2}H incorporation was visualized at ~100-nm spatial resolution, allowing for assignment of activity at the scale of single cells within biofilms at various stages of development. In all cases and redox potentials, the highest anabolic activity occurred at the electrode surface, with a near-linear decrease in activity with distance from the electrode. This distance-dependent decline was also evident in biofilms only a few cells thick, as well as in 2-wk-old biofilms, suggesting that electron transfer over distance, rather than diffusion of nutrients from the medium, is the primary cause of current limitations in these environments.

Results

Metabolic Activity Decreases from the Electrode Surface toward the Outer Edge of the Biofilm. To analyze anabolic activity within current-producing biofilms, *G. sulfurreducens* was grown with graphite electrodes poised at +240 mV vs. standard hydrogen electrode (SHE) as the sole terminal electron acceptor. Prior work has shown that after an initial exponential phase where both cells and current increase at a similar rate, biomass on the electrode continues to increase but current does not, suggesting that only a subset of the biofilm is actively growing (25). We first labeled cells during this characteristic "plateau" phase, when the exponential phase of current production had ceased; 83 h into the experiment, the growth medium was replaced by growth medium containing ^{15}N-enriched ammonium, ^{13}C-enriched acetate, and ^{2}H-enriched water. Current production by biofilms after addition of isotopically labeled medium paralleled those exposed to a regular medium control (Fig. 1*A*).

After an incubation period corresponding to the known doubling time of *G. sulfurreducens* (6.2 ± 0.7 h, $n = 7$), biofilms were fixed, stained, and embedded in resin for imaging by electron microscopy (Fig. 1*B*) and nanoSIMS analysis (Figs. 2 and 3). Biofilms not exposed to isotopes were incubated in isotopically labeled substrates after fixation as a control for nonspecific binding and abiotic incorporation.

Electron microscopy showed biofilms 15- to 20-μm-thick, with cells in the inner layers oriented perpendicular to the electrode surface (Fig. 1*B*; 89 h of growth). Beyond ~10 μm, cells lost this orientation and appeared less tightly packed. These ultrastructural features were similar to those previously demonstrated for *G. sulfurreducens* grown on electrodes (24, 26). Thin sections of resin-embedded biofilms were deposited on silicon wafers and analyzed for ^{13}C/^{12}C, ^{15}N/^{14}N, and ^{2}H/^{1}H stable isotope incorporation.

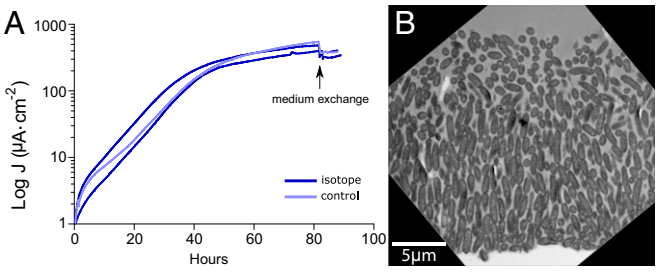

Fig. 1. *G. sulfurreducens* biofilm structure is fully developed as the current density plateau is reached. Current density generation (*A*) and transmission electron microscopy image (*B*) of *G. sulfurreducens* biofilms. Cells were inoculated at time 0 on anodes poised at +240 mV. After 83 h of growth (arrow), normal growth medium was exchanged with stable isotope-labeled medium or unlabeled medium as a control.

In all nanoSIMS analyses, the greatest cellular activity (isotope enrichment) was near the electrode surface, and activity approached zero at a distance >10 μm from the electrode. The $^{14}N^{12}C^-$ ion image was best for visualizing *G. sulfurreducens* biomass because of the lack of nitrogen in the embedding resin (Fig. 2*A*). The heavy nitrogen ion $^{15}N^{12}C^-$, as well as the ^{15}N fractional abundance (^{15}F) images, demonstrate high anabolic activity where cells are adjacent to the anode (Fig. 2 *B* and *C*). This maximum cellular activity at the anode interface decreased with distance to a minimum at 10 μm, followed by a second small peak in cellular anabolic activity close to 15 μm from the electrode. The activity associated with this second peak was more heterogeneous than what was documented near the electrode surface, but was a consistently observed feature under these incubation conditions.

The ^{15}N fractional abundance for all nanoSIMS acquisitions of 3 biological replicates grown at +240 mV is shown in Fig. 2*D*. The features of these isotope enrichment curves within the ∼20-μm biofilm were reproducible, including an early peak in activity at the anode surface, a linear decrease with distance to a minimum isotope enrichment value, and the occurrence of a secondary small peak between this minimum and the outer surface of the biofilm.

The fractional abundances of ^{15}N, ^{13}C, and ^{2}H depicted in Fig. 3 *A*–*C* all showed clear enrichment at the biofilm–anode interface, with ^{15}N, ^{13}C, and ^{2}H incorporation decreasing with distance from the anode surface (Fig. 3). Although these independent isotope tracers will be incorporated in different proportions into the major classes of biomolecules (i.e., lipids, proteins, etc.), the general activity pattern remained the same for ^{13}C, ^{2}H, and ^{15}N enrichment. Here we present data from the ^{15}N enrichment as this yielded the highest signal-to-noise ratio, with little to no exogenous nitrogen in the resin to dilute the signal from the stable isotope probing experiment (57).

With a fractional abundance of ^{15}N added to growth media at 0.06, a *G. sulfurreducens* cell ($^{15}F = 0.0036$) doubling in 6 h would reach an ^{15}N fractional abundance value of ∼0.03 in our experiments, assuming all N came from the added NH_4^+. Consistent with this prediction, peak values of fractional abundance were as high as 0.025 at the anode surface at the end of the 6-h incubation, allowing us to infer that cells closest to the electrode were doubling at nearly their maximum reported rate during the stable isotope probing experiment, even though they were positioned at the base of the biofilm farthest from the growth medium.

Exponentially Growing Biofilms a Few Cell Layers Thick Already Display Anabolic Activity Gradients. Early in growth experiments, when current and biomass are increasing exponentially and biofilms are only ∼5-μm-thick, all cells are hypothesized to be doubling at maximal rates. Samples from this growth phase were analyzed to determine anabolic activity and test if such biofilms showed evidence of metabolic stratification. The thickness of biofilms harvested during this early phase (Fig. 4*A*) ranged between 2 and 4 μm (Fig. 4 *B* and *C*; 35 h of growth), and all exhibited a similar magnitude and trend of isotope incorporation (Fig. 4*D*).

The peak enrichment value, reflecting the maximal growth rate of cells in thin biofilms, was indistinguishable from thicker biofilms. Importantly, the region of fastest growth occurred at the same location in thin biofilms as in older biofilms. This indicated that cells in the upper layers of thick biofilms did not inhibit growth of their brethren at the anode surface, such as by consuming acetate before it diffused to the inner layers, or by acidification. Surprisingly, in these thin biofilms, a decline in metabolic activity was still detected with increasing distance, following the same trend as seen in thicker biofilms. Based on these observations, distance from the anode is a key variable slowing cell growth even at short distances, compared with the presence of additional bacteria or thickness of the biofilm. Additional nanoSIMS images of ^{15}N incorporation and plots for exponential and plateau phase can be found in *SI Appendix*, Fig. S1.

Lowering Redox Potential of the Anode Increases the Gradient in Anabolic Activity. Lowering the redox potential of an anode makes electron transfer by *G. sulfurreducens* less favorable. Under these conditions, the slower metabolic rate of cells could reduce demands on the conductive network or slow consumption of nutrients relative to diffusion into the biofilm, extending the zone where growth is possible. Conversely, if redox potential simply decreases with distance from the anode without a concomitant change in metabolic rate, starting at a lower potential would shrink the region where growth is possible. To directly test how cellular activity patterns were affected by anode potential, we analyzed the isotope incorporation patterns of *G. sulfurreducens* biofilms grown at −100 mV vs. SHE compared with those grown under the more optimal +240 mV. Four separate biofilms were grown at this lower potential, subjected to labeled media at various points during or after exponential current increase to create labeled biofilms ∼5- and ∼15-μm-thick, and analyzed as before with isotope incorporation data binned every half-micron from the surface of the anode (Fig. 5 *A*–*E*).

The major similarity between these biofilms and those grown at +240 mV was the dominant trend of metabolic activity decreasing with distance from the anode surface. However, the decline in activity occurred much more rapidly when the anode potential was lower (−100 mV), with no initial peak in activity. Additionally, the second peak of activity beyond 10 μm was absent, yielding a much simpler pattern which decreased rapidly with distance from the anode. Overall, the use of a lower redox potential reduced the distance from the electrode where activity was detected.

Increased Driving Force at the Electrode Surface Does Not Immediately Change Anabolic Activity Patterns. The difference between biofilms grown at −100 mV vs. +240 mV indicated a strong impact of anode potential on metabolic stratification in biofilms. As many microbial electrochemical systems cycle or shift the anode potential during experiments or treatments, we investigated the ability of these biofilms to respond to a sudden transition in potential. Biofilms were grown at −100 mV until current plateau stage, isotopically labeled growth medium was added as before, and then the electrode potential was changed to the more favorable +240 mV. The resulting ^{15}N fractional abundance plots resembled those grown and labeled at −100 mV, including a steep decrease in isotope incorporation with distance and lack of significant peaks in distant regions of the biofilm (Fig. 5*F*). This indicated that over the short term, the more favorable potential could not be transmitted farther from the anode, or the conductive network in these biofilms could not be remodeled within 6 h, to allow the increased driving force at the base of the biofilm to be used by cells more distant from the electrode as observed in biofilms initiated at +240 mV (Fig. 2).

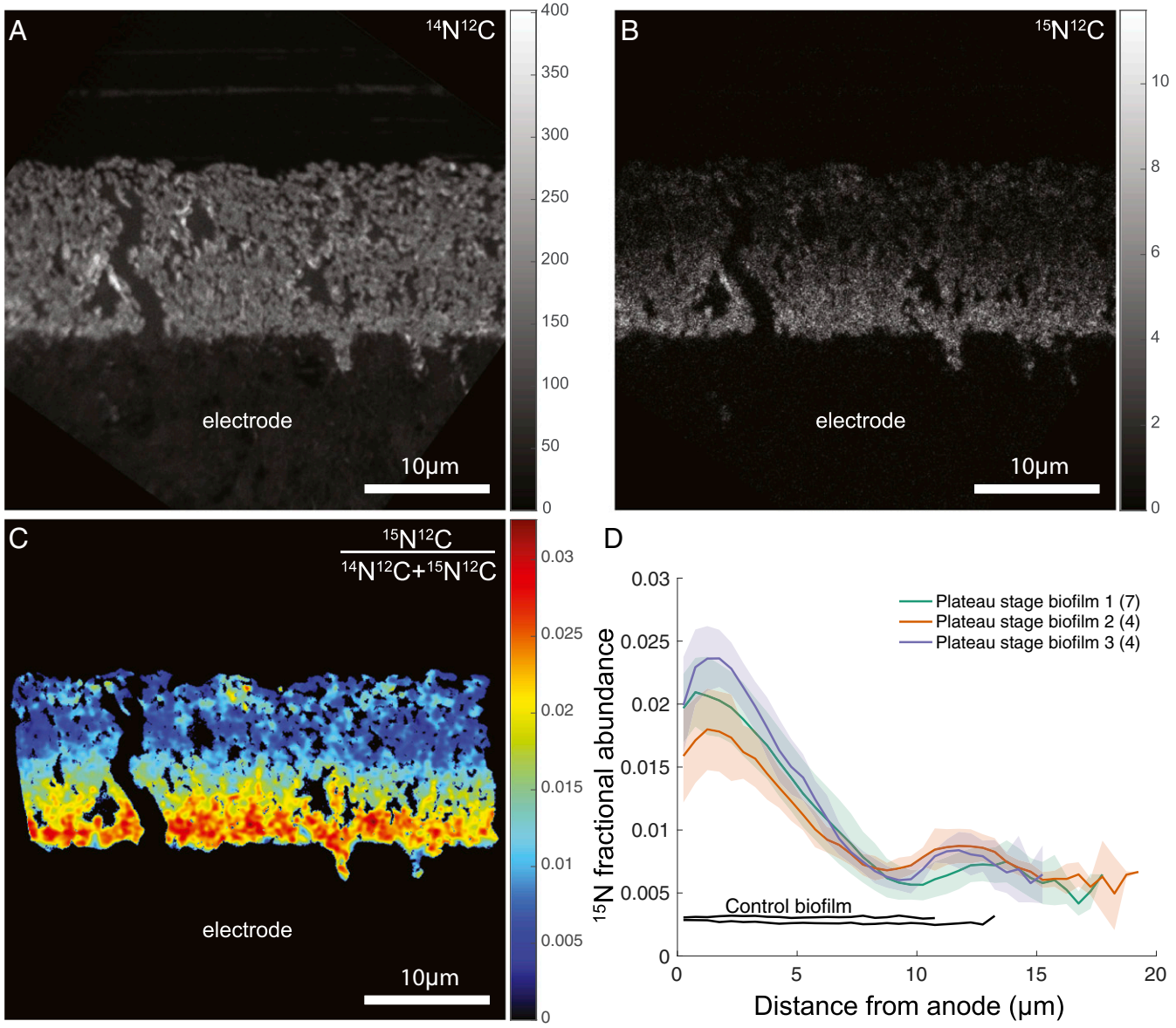

Fig. 2. ^{15}N incorporation reveals anabolic activity patterns within *G. sulfurreducens* biofilms. Representative nanoSIMS analysis of *G. sulfurreducens* biofilms. (*A*) $^{14}N^{12}C^-$ ion image demonstrating biofilm morphology and spatial resolution. The graphite anode is located below the biofilm and the vertical black zone is a crack in the resin. (*B* and *C*) Heavy-nitrogen isotope image $^{15}N^{12}C^-$ (*B*) and ^{15}N fractional abundance image (*C*) reveal an enrichment at the anode surface. Graded scales (*Right*) serve as legends of abundance (*A* and *B*) or fractional abundance (*C*) measured throughout the biofilm. In *C*, only pixels corresponding to the biofilm are displayed (*Materials and Methods*), and a 1-pixel-radius Gaussian blur is applied for image clarity. (*D*) Anabolic activity patterns in replicate *G. sulfurreducens* biofilms ($n = 3$). Colored lines represent the average ^{15}N fractional abundance of different locations within a single biofilm. Transparent envelopes surrounding lines represent the SD of fractional abundance at each distance calculated based on multiple acquisitions of each biofilm (the numbers of acquisitions per biological replicate are shown in parentheses in the legend). Black lines represent controls that were chemically fixed before incubating with isotopically labeled media, indicating live cells are required for isotope incorporation.

Extended Biofilm Operation Does Not Change the Location of Metabolically Active Cells. These results indicate that as biofilms at both high and low redox potentials add additional biomass, cells in the outer layers of the biofilm are at a disadvantage compared with their counterparts at the biofilm–anode interface. After the biofilm reaches a characteristic thickness, additional layers cannot contribute, producing the signature of a constant current plateau. Microbial electrochemical applications often maintain biofilms for weeks in this constant-current mode (23, 28, 29, 31), while the data presented thus far are derived from much younger biofilms. One hypothesis that could explain earlier reports of the majority of live cells located at the top of biofilms is that during longer experiments with thicker biofilms, the activity pattern changes. To test this possibility, 4 replicate *G. sulfurreducens* biofilms were grown for at least 2 wk with normal growth medium on electrodes poised at +240 mV vs. SHE. Unlabeled medium was exchanged as needed to keep nutrient levels in excess and prevent starvation, maintaining current production above 500 $\mu A \cdot cm^{-2}$ for this entire period. After this extended operation, biofilms were supplied with isotopically labeled medium for 6 h and prepared as before.

Electron microscopy revealed much larger biofilms, often over 80 μm in thickness. However, unlike the younger biofilms, cells in top layers of the long-term biofilm showed evidence of lysis or consumption of cellular material, with low cellular electron density documented in all 4 replicates (Fig. 6*A* and *SI Appendix*, Fig. S2). The frequency of intact cells increased with depth into the biofilm

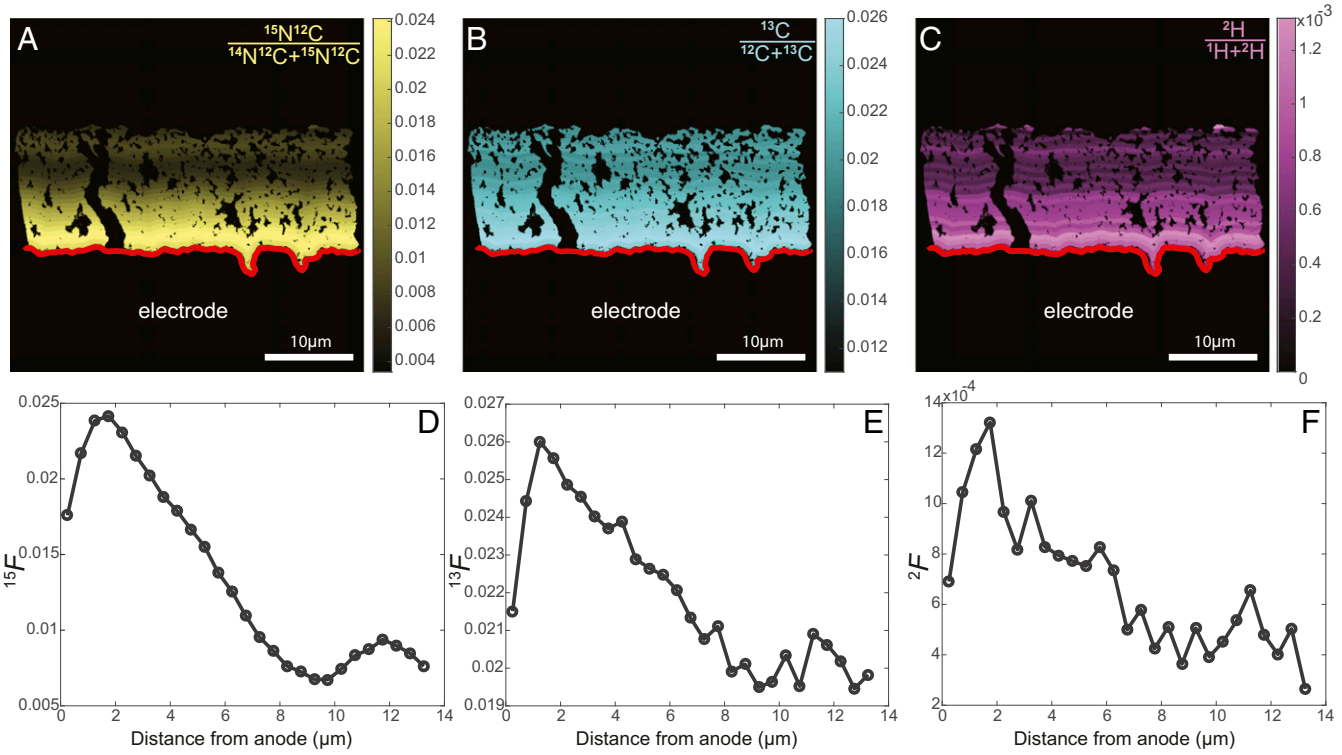

Fig. 3. ^{13}C and ^{2}H incorporation follow the same pattern as ^{15}N. (*A–C*) Fractional abundance of ^{15}N (*A*), ^{13}C (*B*), and ^{2}H (*C*) binned every half-micron from the anode surface (red lines). Graded scales (*Right*) serve as legends of fractional abundance measured throughout the biofilm. (*D–F*) Half-micron binned fractional abundance as a function of distance from the electrode for ^{15}N, ^{13}C, and ^{2}H, respectively, from representative samples.

and, at the anode–biofilm interface, the majority of cells appeared intact, as determined by cell morphology and electron density in the cytoplasm. These patterns were consistent with the measurements of Schrott et al. (31), who found the DNA content of *Geobacter* biofilms increased steadily as biofilms were grown for similar periods of time, but the RNA:DNA ratio dropped sharply, consistent with degradation of anabolic capacity.

Representative nanoSIMS isotope ratio images collected from various positions in the biofilm demonstrated that cells located near the anode were the only bacterial cells showing metabolic activity. Despite the large amount of cell mass in the upper portion of the biofilm, the peak activity level near the electrode was similar to those measured for 5- and 15-μm-thick biofilms (Fig. 6*B*). Cells in outer layers, far from the anode, showed very little evidence of anabolic activity, with only occasional weak cellular enrichment signals. Consistent with our interpretation of cell lysis in upper layers, cells with higher electron density also contained substantially higher $^{14}N^{12}C$ counts relative to the top of the biofilm, reflecting high cellular concentrations of nitrogen-containing biomolecules in cells adjacent to the electrode (Fig. 6*A* and *SI Appendix*, Fig. S2). These results indicated that for consistently poised and maintained electrode biofilms, active growth continued near the electrode surface, pushing older cells out to the biofilm–medium interface, with surprisingly no apparent inhibition or contribution from nearly 80 μm of cells above the active layer.

Are Cellular Activity Profiles Due to Cell Growth Only at the Electrode Surface? Our isotope labeling experiments were conducted within an estimated doubling of *G. sulfurreducens* to minimize the potential for altering cellular activity–distance profiles due to active cell division; however, it is possible that cells at the anode surface are dividing faster than the 6-h labeling. To verify that the observed activity patterns in our experiments represent snapshots of cellular activity within communities that are spatially stable during the labeling period, we performed incubations in which biofilms were labeled for approximately 2 h with 3 times the level of isotope enrichment added to the medium. In this experiment, nanoSIMS analysis of a biofilm with similar final current densities as those presented in Figs. 2 and 3 produced a similar activity profile after only a 2-h isotope pulse (~1/3 of a doubling), demonstrating that the observed pattern of isotope enrichment was not simply due to physical displacement of *Geobacter* cells from the electrode surface during biofilm growth but rather is an activity profile that represents cells having lower anabolic activity as distance from the electrode increases (*SI Appendix*, Fig. S3).

Can *Geobacter* Respire in the Absence of Anabolic Activity? The incorporation of isotopically labeled substrates requires synthesis of new cellular material from N, C, or H, and it is important to consider that some cells could actively respire and contribute to current production but not actively divide. Fast-growing heterotrophs like *Streptococcus* and *Escherichia coli* have well-documented abilities to uncouple catabolic from anabolic metabolism (58), but this is less well documented in bacteria during extracellular respiration. To examine the capacity of *G. sulfurreducens* to produce current in the absence of anabolic activity, we treated plateau-stage biofilms with tetracycline, an inhibitor of protein synthesis. In the presence of excess acetate and other nutrients, current production by tetracycline-treated biofilms decreased 95%. When medium was replaced to wash tetracycline from the biofilms, respiration recovered to near-original levels. These experiments suggested that current production and anabolic activity were tightly coupled in these biofilms (*SI Appendix*, Fig. S4).

Discussion

The results presented here demonstrate that *G. sulfurreducens* biofilms experience a growth penalty with increasing distance from

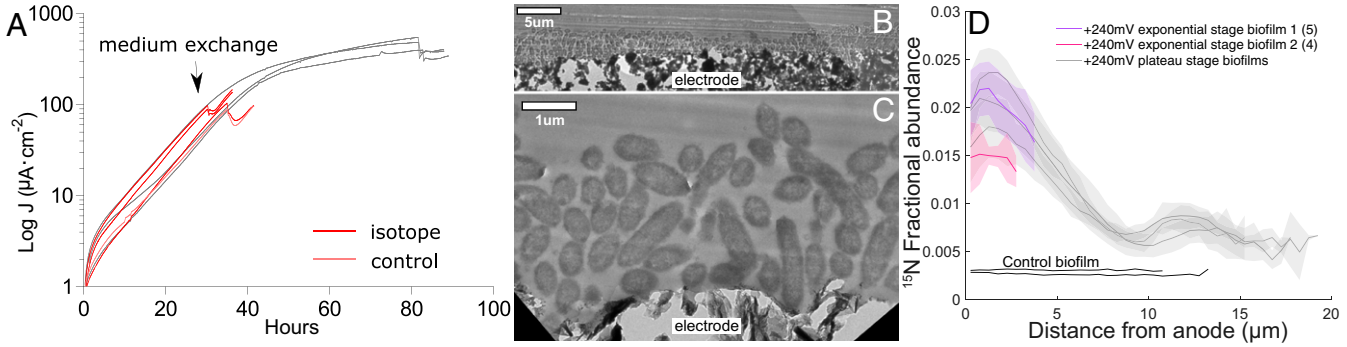

Fig. 4. Decrease in anabolic activity with distance from the electrode is already present in thin biofilms. (*A*–*C*) Current density (*A*) and transmission electron microscopy images (*B* and *C*) of representative *G. sulfurreducens* biofilms harvested during exponential phase. Graphite electrodes poised at +240 mV vs. SHE served as the terminal electron acceptor, and normal growth media were exchanged with stable isotope-labeled media after 35 h of growth (arrow in *A*). (*D*) Anabolic activity patterns in duplicate *G. sulfurreducens* biofilms. Red and purple lines represent the average ^{15}N fractional abundance at different locations within a single biofilm (the numbers of acquisitions per biological replicate are shown in parentheses in the legend). Transparent envelopes surrounding lines represent the SD of fractional abundance at each distance. Black lines represent controls that were chemically fixed before incubating with isotopically labeled media. For comparison, data from *A* and *D* are overlaid on data in gray from Figs. 1*A* and 2*D*, respectively, to show the similar maximum and decrease with distance features.

the anode surface. This result is robust at both the level of biofilm maturation and the reduction potential of the anode. A similar rate of ^{15}N incorporation is observed in cells near the anode surface during exponential phase and in thick biofilms after current plateau, indicating that cells in the upper layers of the biofilm do not significantly inhibit inner layers by consuming substrate or producing toxic byproducts. This pattern, with anabolic activity dominating a relatively narrow zone at the anode surface, was true even after weeks of biofilm growth, indicating that the dominant synthesis of new biomass throughout all stages occurs at the anode, pushing old inactive biomass outward. This also shows that cells inside the biofilm continue to grow exponentially even as the current production rate of the biofilm as a whole reaches "stationary phase." Thus, current-producing

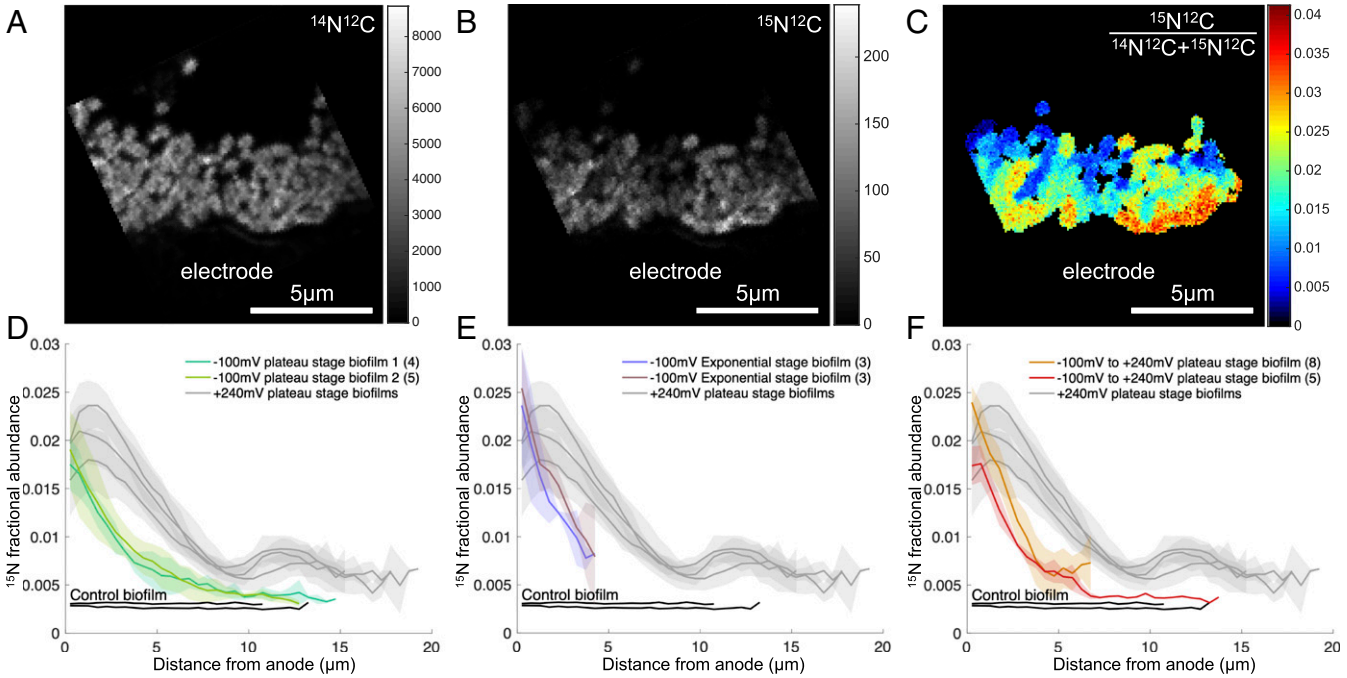

Fig. 5. Lowering the poised potential of electrodes causes anabolic activity of *G. sulfurreducens* to decrease even more rapidly with distance, and cannot be restored by exposure to a more favorable reduction potential. Representative nanoSIMS analysis of *G. sulfurreducens* biofilms grown with graphite electrodes poised at −100 mV vs. SHE as the sole terminal electron acceptor. (*A*) ^{14}N^{12}C$^-$ ion image demonstrating biofilm morphology and spatial resolution. The graphite anode is located in the bottom, below the biofilm. (*B* and *C*) Heavy-nitrogen isotope image ^{15}N^{12}C$^-$ (*B*) and ^{15}N fractional abundance image (*C*) reveal an enrichment at the anode surface. Graded scales (*Right*) serve as legends of fractional abundance measured throughout the biofilm. In *C*, only pixels corresponding to the biofilm are displayed (*Materials and Methods*). (*D*–*F*) Anabolic activity patterns in replicate *G. sulfurreducens* biofilms grown with graphite electrodes poised at −100 mV vs. SHE as the sole terminal electron acceptor and harvested once current reached plateau (*D*), during exponential phase (*E*), or once current reached plateau and the reduction potential of the working electrode was raised to +240 mV vs. SHE for the duration of isotope label incorporation (*F*). Lines represent the average ^{15}N fractional abundance for analyses of different locations within a single biofilm (the numbers of acquisitions per biological replicate are shown in parentheses in the legend). Transparent envelopes surrounding lines represent the SD of fractional abundance at each distance. Black lines represent controls that were chemically fixed before incubating with isotopically labeled medium. For comparison, data from *D*–*F* are overlaid on data in gray from Fig. 2*D*.

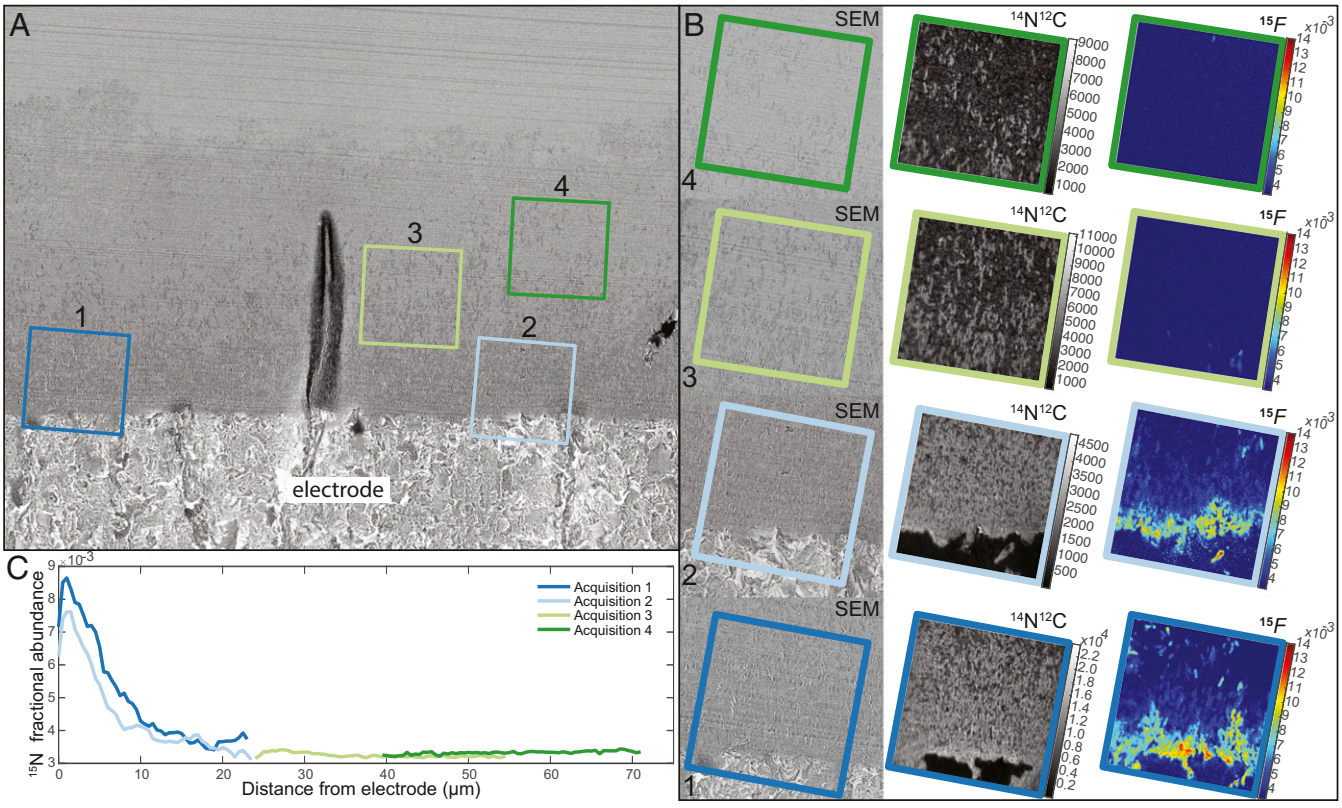

Fig. 6. Anabolic activity pattern of *G. sulfurreducens* biofilms does not change after growth is maintained for 2 wk. (*A*) Electron microscopy and nanoSIMS analysis of a representative 2-wk-old biofilm. Scanning electron microscopy image showing a 2-wk-old biofilm grown at +240 mV, demonstrating the thickness of the biofilm and regions of cell lysis in the upper layers. Representative nanoSIMS images were taken in regions 1 to 4. (*B*) The $^{14}N^{12}C^-$ ion image is shown along with the ^{15}N fractional abundance for each region next to their enlarged SEM image. (*C*) Anabolic activity patterns in 2-wk-old *G. sulfurreducens* biofilms. Dark blue, light blue, light green, and dark green represent the ^{15}N fractional abundance for analyses of regions 1, 2, 3, and 4, respectively. Data are representative of 3 biological replicates. Acquisition regions are 30-μm-square and serve as scale bars.

biofilms are not a monolithic and homogeneous entity but varied and heterogeneous, with metabolically stratified regions. This heterogeneity has implications for transcriptional, proteomic, and metagenomic studies that treat entire biofilms as a single community.

The transition from an exponential increase in current to a plateau phase correlates with our findings of 2 major physiological regions within the biofilm. First, our results show that at distances of ∼10 μm from the anode, anabolic activity is reduced to a minimum, regardless of the potential at which the electrode is poised. Second, the regular orientation of the cells perpendicular to the anode surface breaks down at approximately this same point. Biofilms grown at high potential do continue to increase total current at a slow but steady rate (Fig. 1*A*), and exhibit a previously unrecognized secondary zone of modest anabolic activity in outermost layers (Fig. 2*D*), while low-potential biofilms do not exhibit any further current increase within this secondary zone (Fig. 5 *A*–*D*).

Our nanoSIMS activity data agree with redox potential and cytochrome oxidation state measurements, and studies finding significant differences between the inner ∼10 μm of these biofilms vs. outer layers (26, 33, 38). Specifically, previous results using viability or respiratory stains suggested that while cells are alive throughout the biofilm, outer layers had different metabolic rates based on transcriptional profiles (38) or changes in protein abundance (24, 26). These previous results are consistent with the anabolic gradient presented in Fig. 2, producing a quantitative measure of what were previously qualitative observations. Cells appear to only experience the set potential near the anode surface, while cells located farther from electrodes experience an increasingly reduced pool of extracellular cytochromes to act as their electron acceptor (40–45, 59), which ultimately makes electron transfer unfavorable to support growth. The low redox potential in these outer layers still appears to allow some acetate oxidation to proceed, based on the slow increase in current that occurs over subsequent days to weeks. We hypothesize that the second zone of anabolic activity in this region >10 μm from the electrode represents a shift to a low potential-specific mode of growth, enabled by recently discovered systems such as the quinol oxidase CbcL that operates around potentials of −100 mV (50). The fact that electrode surfaces poised at potentials near −100 mV fail to develop a distant zone of growth supports this model, as potential should more rapidly decrease to an unfavorable value in these biofilms. Alternatively, this second increase in anabolic activity could represent a switch to reliance on long-range electron transfer pathways such as those previously proposed to be dependent on the presence of cytochrome polymers (36) and/or pili (32, 33).

These data represent a direct quantitative measurement of *G. sulfurreducens* anabolic activity at high spatial resolution within conductive biofilms. Our results highlight the uniqueness of current-producing biofilms, which stratify in a different pattern from canonical biofilm models, with the most anabolically active cells in bottom layers where dead or persister cells are typically found (1, 2). The combined effect of factors that could limit cellular metabolism within electroactive biofilms favors growth at the biofilm–anode interface. Localization of

the most active cells at the electrode interface dispels the notion that pH or substrate limitation strongly inhibits growth of cells in the inner layers of these biofilms, despite models predicting such an effect (44–47). In fact, in some cases, the highest rates of growth occurred within pockets or pits inside the graphite electrodes, where diffusion to cells was most severely restricted (i.e., *SI Appendix*, Fig. S1*A*). While these data cannot resolve which components enable extracellular electron transfer, our results constrain future models to ones that account for the major mode of biofilm growth occurring in layers near the anode, that push biomass outward into increasingly less favorable conditions.

These results support the widely held conclusion that *G. sulfurreducens* biofilms are conductive at distances exceeding 10 μm, but reveal that "metabolism at a distance" comes with a cost, which is eventually inhibitory to growth. While the exact pattern of activity will vary between reactor designs, substrate concentrations, and especially buffering capacity of the media, the data presented here can be used to reconcile conflicting models of electroactive biofilms. Follow-up studies using mutants lacking conductive appendages such as polymerized OmcS cytochromes (36), or redox potential-specific oxidases such as CbcL, could test new predictions regarding the molecular basis for growth within biofilms. With the growing number of environmental Bacteria and Archaea shown to be capable of direct extracellular electron transfer, either for microbial growth on metal oxide materials or to mediate syntrophic growth between microbes (e.g., refs. 22, 60, 61), enhancing our mechanistic understanding of growth by current-producing microorganisms is an important goal of environmental microbiology. Our findings place limitations on the extracellular electron transfer process and help constrain the extent to which it can support active cell growth in these increasingly important microbial systems.

Materials and Methods

***Geobacter* Growth.** All experiments were performed using our laboratory strain of *G. sulfurreducens* PCA, with each experiment using freshly streaked single colonies from freezer stocks. Anaerobic NB medium (0.38 g/L KCl, 0.2 g/L NH_4Cl, 0.069 g/L $NaH_2PO_4H_2O$, 0.04 g/L $CaCl_2 2H_2O$, 0.2 g/L $MgSO_4 7H_2O$, 1% [vol/vol] trace mineral mix, pH 6.8, buffered with 2 g/L $NaHCO_3$ and flushed with oxygen-free 80:20 N_2:CO_2 gas mix) with 20 mM acetate as electron donor and 40 mM fumarate as electron acceptor was used to grow liquid cultures from colony picks; 3-cm^2 graphite electrodes were polished using 1500-grade sand paper (Gator Finishing Products) followed by a 0.05-μm alumina slurry (Buehler), and cleaned via sonication to serve as working electrodes. Sterile 3-electrode conical reactors containing 15 mL acceptor-free medium with 40 mM acetate as the electron donor and 50 mM NaCl to equilibrate salt concentrations were flushed with a mix of N_2:CO_2 gas (80:20, vol/vol) until the O_2 concentration reached less than 2 ppm. Cultures were prepared by inoculating multiple 1-mL liquid cultures from different single colonies inside an anaerobic chamber. Once these cultures reached late exponential phase, they were used to inoculate separate 10-mL cultures with 10% (vol/vol). Each reactor was then inoculated with 25% (vol/vol) from this liquid culture as it approached acceptor limitation (as it reached an OD_{600} of 0.48). Working electrodes were set at either −100 or +240 mV vs. standard hydrogen electrode and average current density was recorded every 12 s. All experiments were carried out at 30 °C.

Stable Isotope Probe Medium. Heavy isotope-labeled medium was identical in chemical composition to normal growth medium, with an increase in the final heavy isotope of ^{15}N to 6 atom% in ammonium, ^{13}C to 6 atom% in both acetate carbons, and ^{2}H to 2 atom% in water. Enriched isotopic chemicals were purchased from Cambridge Isotope ($^{15}NH_4Cl$ [NLM-467]) and Sigma (D_2O [151882]; $^{13}CH_3{}^{13}CO_2Na$ [282014]). Increased strength-labeled media for short-term incubations were made using 3× the heavy-isotope percentage with identical concentrations of chemical species.

Stable Isotope Probing. Once the desired biofilm growth stage had been reached, the potentiostat was paused, and medium was carefully exchanged for 15 mL labeled medium. For negative control samples, regular electrode growth medium was used instead of stable isotope-enriched medium. Biofilms were then incubated for 6 h with working electrodes poised at the same potential as during growth, or changed from −100 to +240 mV (Fig. 5*F*).

Fixation and Embedding. After stable isotope incubation, graphite electrodes were harvested from each reactor, rinsed by placing in fresh medium once to remove planktonic cells, fixed at room temperature for 1 h (2% glutaraldehyde, 50 mM Hepes, pH 6.8), and stored at 4 °C in fixing solution. Negative controls to test for nonspecific isotope binding were rinsed and incubated for 6 h in stable isotope-enriched media before storing in fixative. Samples (still attached to graphite) were rinsed twice (50 mM Hepes, pH 7) before negative staining in 1% OsO_4, 50 mM Hepes (pH 7) for 2 h. After rinsing again, samples were incubated for 1 h in 1% uranyl-acetate and rinsed. Samples were then dehydrated with sequential 10-min incubations in 25, 50, 75, and 100% EtOH. A 50/50 (vol/vol) LR White resin (Sigma-Aldrich; uncatalyzed) and EtOH solution were used to incubate samples at room temperature overnight. Samples were then placed in 2-mL microcentrifuge tubes containing enough LR White solution (catalyzed with benzoyl peroxide) to cover ∼0.5 cm above the graphite flag (∼1.5 mL) and incubated at 60 °C overnight.

Sample Preparation for NanoSIMS. Resin-embedded biofilm-covered electrodes were cut perpendicular to the largest face of the electrode with a jeweler's saw, and a smooth face was prepared using a microtome and glass knife. Thin sections between 200 and 500 nm were cut for nanoSIMS analysis with a diamond knife. Floated sections were collected on glow-discharged 7- × 7-mm silicon wafers (Active Business). Sections on silicon wafers were coated with 40-nm gold using a Cressington sputter coater.

Electron Microscopy. A subset of biofilm sections were imaged with transmission and scanning electron microscopy (TEM and SEM). For TEM, 100-nm sections were cut using a diamond knife, collected on copper TEM grids, and imaged on an FEI Tecnai (T12) operated at 120 keV. Sections collected on silicon wafers (described above) were imaged on a Merlin Compact scanning electron microscope (Zeiss).

NanoSIMS Data Acquisition. Isotope enrichment data were collected on a CAMECA nanoSIMS 50L housed in the Center for Microanalysis at the California Institute of Technology. Gold-coated samples were presputtered with a 90-pA primary Cs^+ ion beam with aperture diaphragm D1 = 1 until the $^{14}N^{12}C^-$ ion counts stabilized. Data were collected using a 0.5-pA beam with D1 = 3 and entrance slit (ES) = 2. Six masses were collected corresponding to the $^{1}H^-$, $^{2}H^-$, $^{12}C^-$, $^{13}C^-$, $^{14}N^{12}C^-$, and $^{15}N^{12}C^-$ ions, for the determination of $^{2}H/^{1}H$, $^{13}C/^{12}C$, and $^{15}N/^{14}N$ ratios, respectively, using a tuning similar to that described in Kopf et al. (57). Acquisitions were 10- to 40-μm-square raster areas, with 128 × 128 to 512 × 512 pixels, and 1 to 4 planes were collected per area. Dwell time settings resulted in acquisition times from 25 min to 2 h per plane depending on the size of the rasters.

Data Processing. NanoSIMS.im data files were initially processed using the Look@NanoSIMS Matlab GUI (62) to align planes and export raw data. All subsequent data processing and analysis were done in Matlab. Regions of acquisitions that contained *Geobacter* biofilm were outlined on the $^{14}N^{12}C^-$ mass image, where the surface of the electrode was traced by hand, and each pixel of *Geobacter* biofilm was assigned a minimum distance to the electrode surface by calculating the pairwise distance between each pixel in the biofilm and the electrode surface. Biofilm pixels were assigned to bins of 0.5-μm increments from the anode surface, and the $^{15}N^{12}C^-$ and $^{14}N^{12}C^-$ counts were pooled for each distance bin to calculate the fractional abundance of the heavy isotopes: $^{15}F = {}^{15}N^{12}C^-/({}^{15}N^{12}C^- + {}^{14}N^{12}C^-)$. Pixels with low $^{14}N^{12}C$ counts corresponding to the epoxy resin in-between cells were omitted, as was the farthest-distance bin when it contained very few pixels.

ACKNOWLEDGMENTS. This publication was supported by the US Department of Energy, Office of Science, Office of Biological and Environmental Research (DE-SC0016469) and the NASA Astrobiology Institute, Award NNA13AA92A (to V.J.O.) and the Simons Foundation (Program: Life Sciences-Simons Collaboration on Principles of Microbial Ecosystems; Award 542393). D.R.B. and J.A.G. were supported by National Science Foundation Dimensions of Biodiversity program DEB 1542513. G.L.C. was supported by NIH/NRSA Training Grant T32 GM007616. F.J.O. was supported by the Mexican National Council for Science and Technology and the Office of Naval Research Award N000141612194. We thank Dr. Gail Celio for training and loan of the UMN Imaging facilities, Dr. Ryan Hunter for assistance developing a biofilm staining and embedding protocol, and Dr. Yunbin Guan for assistance with the nanoSIMS analysis.

1. P. Stoodley, K. Sauer, D. G. Davies, J. W. Costerton, Biofilms as complex differentiated communities. *Annu. Rev. Microbiol.* **56**, 187–209 (2002).
2. H.-C. Flemming *et al*., Biofilms: An emergent form of bacterial life. *Nat. Rev. Microbiol.* **14**, 563–575 (2016).
3. C. J. Tadanier, M. E. Schreiber, J. W. Roller, Arsenic mobilization through microbially mediated deflocculation of ferrihydrite. *Environ. Sci. Technol.* **39**, 3061–3068 (2005).
4. H. L. Ehrlich, "Uppermost lithosphere as a microbial habitat" in *Ehrlich's Geomicrobiology*, H. L. Ehrlich, D. K. Newman, A. Kappler, Eds. (CRC Press, Boca Raton, FL, ed. 6, 2015), pp. 55–68.
5. T. J. Battin, L. A. Kaplan, J. Denis Newbold, C. M. E. Hansen, Contributions of microbial biofilms to ecosystem processes in stream mesocosms. *Nature* **426**, 439–442 (2003).
6. F. S. Islam *et al*., Role of metal-reducing bacteria in arsenic release from Bengal delta sediments. *Nature* **430**, 68–71 (2004).
7. C. J. Gantzer, B. E. Rittmann, E. E. Herricks, Mass transport to streambed biofilms. *Water Res.* **22**, 709–722 (1988).
8. D. S. Domozych, C. R. Domozych, Desmids and biofilms of freshwater wetlands: Development and microarchitecture. *Microb. Ecol.* **55**, 81–93 (2008).
9. N. B. Ramsing, M. Kühl, B. B. Jørgensen, Distribution of sulfate-reducing bacteria, O_2, and H_2S in photosynthetic biofilms determined by oligonucleotide probes and microelectrodes. *Appl. Environ. Microbiol.* **59**, 3840–3849 (1993).
10. P. Stoodley, I. Dodds, J. D. Boyle, H. M. Lappin-Scott, Influence of hydrodynamics and nutrients on biofilm structure. *J. Appl. Microbiol.* **85** (suppl. 1), 19S–28S (1998).
11. D. de Beer, P. Stoodley, F. Roe, Z. Lewandowski, Effects of biofilm structures on oxygen distribution and mass transport. *Biotechnol. Bioeng.* **43**, 1131–1138 (1994).
12. K. Sauer, A. K. Camper, G. D. Ehrlich, J. W. Costerton, D. G. Davies, Pseudomonas aeruginosa displays multiple phenotypes during development as a biofilm. *J. Bacteriol.* **184**, 1140–1154 (2002).
13. P. Wilmes *et al*., Natural acidophilic biofilm communities reflect distinct organismal and functional organization. *ISME J.* **3**, 266–270 (2009).
14. R. Lemaire, R. I. Webb, Z. Yuan, Micro-scale observations of the structure of aerobic microbial granules used for the treatment of nutrient-rich industrial wastewater. *ISME J.* **2**, 528–541 (2008).
15. T. H. J. A. Sleutels, A. Ter Heijne, C. J. N. Buisman, H. V. M. Hamelers, Bioelectrochemical systems: An outlook for practical applications. *ChemSusChem* **5**, 1012–1019 (2012).
16. D. R. Bond, D. E. Holmes, L. M. Tender, D. R. Lovley, Electrode-reducing microorganisms that harvest energy from marine sediments. *Science* **295**, 483–485 (2002).
17. L. M. Tender *et al*., Harnessing microbially generated power on the seafloor. *Nat. Biotechnol.* **20**, 821–825 (2002).
18. D. E. Holmes *et al*., Microbial communities associated with electrodes harvesting electricity from a variety of aquatic sediments. *Microb. Ecol.* **48**, 178–190 (2004).
19. S. Jung, J. M. Regan, Comparison of anode bacterial communities and performance in microbial fuel cells with different electron donors. *Appl. Microbiol. Biotechnol.* **77**, 393–402 (2007).
20. H.-S. Lee, P. Parameswaran, A. Kato-Marcus, C. I. Torres, B. E. Rittmann, Evaluation of energy-conversion efficiencies in microbial fuel cells (MFCs) utilizing fermentable and non-fermentable substrates. *Water Res.* **42**, 1501–1510 (2008).
21. S. Tejedor-Sanz, P. Fernández-Labrador, S. Hart, C. I. Torres, A. Esteve-Núñez, Geobacter dominates the inner layers of a stratified biofilm on a fluidized anode during brewery wastewater treatment. *Front. Microbiol.* **9**, 378 (2018).
22. Z. M. Summers *et al*., Direct exchange of electrons within aggregates of an evolved syntrophic coculture of anaerobic bacteria. *Science* **330**, 1413–1415 (2010).
23. D. Sun *et al*., Temporal-spatial changes in viabilities and electrochemical properties of anode biofilms. *Environ. Sci. Technol.* **49**, 5227–5235 (2015).
24. K. Inoue *et al*., Specific localization of the c-type cytochrome OmcZ at the anode surface in current-producing biofilms of Geobacter sulfurreducens. *Environ. Microbiol. Rep.* **3**, 211–217 (2011).
25. E. Marsili, J. B. Rollefson, D. B. Baron, R. M. Hozalski, D. R. Bond, Microbial biofilm voltammetry: Direct electrochemical characterization of catalytic electrode-attached biofilms. *Appl. Environ. Microbiol.* **74**, 7329–7337 (2008).
26. C. S. Stephen, E. V. LaBelle, S. L. Brantley, D. R. Bond, Abundance of the multiheme c-type cytochrome OmcB increases in outer biofilm layers of electrode-grown Geobacter sulfurreducens. *PLoS One* **9**, e104336 (2014).
27. P. S. Bonanni, D. F. Bradley, G. D. Schrott, J. P. Busalmen, Limitations for current production in Geobacter sulfurreducens biofilms. *ChemSusChem* **6**, 711–720 (2013).
28. D. Sun *et al*., The effect of biofilm thickness on electrochemical activity of Geobacter sulfurreducens. *Int. J. Hydrogen Energy* **41**, 16523–16528 (2016).
29. D. Sun, S. Cheng, F. Zhang, B. E. Logan, Current density reversibly alters metabolic spatial structure of exoelectrogenic anode biofilms. *J. Power Sources* **356**, 566–571 (2017).
30. K. P. Nevin *et al*., Power output and columbic efficiencies from biofilms of Geobacter sulfurreducens comparable to mixed community microbial fuel cells. *Environ. Microbiol.* **10**, 2505–2514 (2008).
31. G. D. Schrott, M. V. Ordoñez, L. Robuschi, J. P. Busalmen, Physiological stratification in electricity-producing biofilms of Geobacter sulfurreducens. *ChemSusChem* **7**, 598–603 (2014).
32. G. Reguera *et al*., Biofilm and nanowire production leads to increased current in Geobacter sulfurreducens fuel cells. *Appl. Environ. Microbiol.* **72**, 7345–7348 (2006).
33. R. J. Steidl, S. Lampa-Pastirk, G. Reguera, Mechanistic stratification in electroactive biofilms of Geobacter sulfurreducens mediated by pilus nanowires. *Nat. Commun.* **7**, 12217 (2016).
34. A. E. Franks, R. H. Glaven, D. R. Lovley, Real-time spatial gene expression analysis within current-producing biofilms. *ChemSusChem* **5**, 1092–1098 (2012).
35. C. Kirchhoff, H. Cypionka, Propidium ion enters viable cells with high membrane potential during live-dead staining. *J. Microbiol. Methods* **142**, 79–82 (2017).
36. F. Wang *et al*., Structure of microbial nanowires reveals stacked hemes that transport electrons over micrometers. *Cell* **177**, 361–369.e10 (2019).
37. J. B. Rollefson, C. S. Stephen, M. Tien, D. R. Bond, Identification of an extracellular polysaccharide network essential for cytochrome anchoring and biofilm formation in Geobacter sulfurreducens. *J. Bacteriol.* **193**, 1023–1033 (2011).
38. A. E. Franks, K. P. Nevin, R. H. Glaven, D. R. Lovley, Microtoming coupled to microarray analysis to evaluate the spatial metabolic status of Geobacter sulfurreducens biofilms. *ISME J.* **4**, 509–519 (2010).
39. A. Jain, G. Gazzola, A. Panzera, M. Zanoni, E. Marsili, Visible spectroelectrochemical characterization of Geobacter sulfurreducens biofilms on optically transparent indium tin oxide electrode. *Electrochim. Acta* **56**, 10776–10785 (2011).
40. Y. Liu, H. Kim, R. R. Franklin, D. R. Bond, Linking spectral and electrochemical analysis to monitor c-type cytochrome redox status in living Geobacter sulfurreducens biofilms. *ChemPhysChem* **12**, 2235–2241 (2011).
41. L. Robuschi *et al*., Spectroscopic slicing to reveal internal redox gradients in electricity-producing biofilms. *Angew. Chem. Int. Ed. Engl.* **52**, 925–928 (2013).
42. N. Lebedev, S. M. Strycharz-Glaven, L. M. Tender, Spatially resolved confocal resonant Raman microscopic analysis of anode-grown Geobacter sulfurreducens biofilms. *ChemPhysChem* **15**, 320–327 (2014).
43. L. Robuschi, J. P. Tomba, J. P. Busalmen, Proving Geobacter biofilm connectivity with confocal Raman microscopy. *J. Electroanal. Chem. (Lausanne)* **793**, 99–103 (2017).
44. J. T. Babauta, H. D. Nguyen, T. D. Harrington, R. Renslow, H. Beyenal, pH, redox potential and local biofilm potential microenvironments within Geobacter sulfurreducens biofilms and their roles in electron transfer. *Biotechnol. Bioeng.* **109**, 2651–2662 (2012).
45. A. E. Franks *et al*., Novel strategy for three-dimensional real-time imaging of microbial fuel cell communities: Monitoring the inhibitory effects of proton accumulation within the anode biofilm. *Energy Environ. Sci.* **2**, 113–119 (2009).
46. C. I. Torres, A. Kato Marcus, B. E. Rittmann, Proton transport inside the biofilm limits electrical current generation by anode-respiring bacteria. *Biotechnol. Bioeng.* **100**, 872–881 (2008).
47. R. Renslow *et al*., Metabolic spatial variability in electrode-respiring Geobacter sulfurreducens biofilms. *Energy Environ. Sci.* **6**, 1827–1836 (2013).
48. A. Kato Marcus, C. I. Torres, B. E. Rittmann, Conduction-based modeling of the biofilm anode of a microbial fuel cell. *Biotechnol. Bioeng.* **98**, 1171–1182 (2007).
49. C. E. Levar, C. H. Chan, M. G. Mehta-Kolte, D. R. Bond, An inner membrane cytochrome required only for reduction of high redox potential extracellular electron acceptors. *MBio* **5**, e02034 (2014).
50. L. Zacharoff, C. H. Chan, D. R. Bond, Reduction of low potential electron acceptors requires the CbcL inner membrane cytochrome of Geobacter sulfurreducens. *Bioelectrochemistry* **107**, 7–13 (2016).
51. C. E. Levar, C. L. Hoffman, A. J. Dunshee, B. M. Toner, D. R. Bond, Redox potential as a master variable controlling pathways of metal reduction by Geobacter sulfurreducens. *ISME J.* **11**, 741–752 (2017).
52. T. K. Teal, D. P. Lies, B. J. Wold, D. K. Newman, Spatiometabolic stratification of Shewanella oneidensis biofilms. *Appl. Environ. Microbiol.* **72**, 7324–7330 (2006).
53. E. Marsili, J. Sun, D. R. Bond, Voltammetry and growth physiology of Geobacter sulfurreducens biofilms as a function of growth stage and imposed electrode potential. *Electroanalysis* **22**, 865–874 (2010).
54. Z. F. Hallberg *et al*., Structure and mechanism of a Hypr GGDEF enzyme that activates cGAMP signaling to control extracellular metal respiration. *eLife* **8**, e43959 (2019).
55. F. Jiménez Otero, C. H. Chan, D. R. Bond, Identification of different putative outer membrane electron conduits necessary for Fe(III) citrate, Fe(III) oxide, Mn(IV) oxide, or electrode reduction by Geobacter sulfurreducens. *J. Bacteriol.* **200**, e00347-18 (2018).
56. S. H. Kopf *et al*., Trace incorporation of heavy water reveals slow and heterogeneous pathogen growth rates in cystic fibrosis sputum. *Proc. Natl. Acad. Sci. U.S.A.* **113**, E110–E116 (2016).
57. S. H. Kopf *et al*., Heavy water and ^{15}N labelling with nanoSIMS analysis reveals growth rate-dependent metabolic heterogeneity in chemostats. *Environ. Microbiol.* **17**, 2542–2556 (2015).
58. J. B. Russell, G. M. Cook, Energetics of bacterial growth: Balance of anabolic and catabolic reactions. *Microbiol. Rev.* **59**, 48–62 (1995).
59. R. M. Snider, S. M. Strycharz-Glaven, S. D. Tsoi, J. S. Erickson, L. M. Tender, Long-range electron transport in Geobacter sulfurreducens biofilms is redox gradient-driven. *Proc. Natl. Acad. Sci. U.S.A.* **109**, 15467–15472 (2012).
60. S. E. McGlynn, G. L. Chadwick, C. P. Kempes, V. J. Orphan, Single cell activity reveals direct electron transfer in methanotrophic consortia. *Nature* **526**, 531–535 (2015).
61. G. Wegener, V. Krukenberg, D. Riedel, H. E. Tegetmeyer, A. Boetius, Intercellular wiring enables electron transfer between methanotrophic archaea and bacteria. *Nature* **526**, 587–590 (2015).
62. L. Polerecky *et al*., Look@NanoSIMS—A tool for the analysis of nanoSIMS data in environmental microbiology. *Environ. Microbiol.* **14**, 1009–1023 (2012).